12-21-2019

Assessing Magnetic Iron Oxide Nanoparticles Properties under Different Thermal Treatments

Erick S. Vasquez
University of Dayton, evasquez1@udayton.edu

Evan M. Prehn
Texas A&M University

Keisha B. Walters
University of Oklahoma

ASSESSING MAGNETIC IRON OXIDE NANOPARTICLES PROPERTIES UNDER DIFFERENT THERMAL TREATMENTS

Erick S. Vasquez[1,*], Evan M. Prehn[2], Keisha B. Walters[3,*]

1. Department of Chemical and Materials Engineering, University of Dayton, Dayton, OH 45469-0256, USA
2. Department of Materials Science and Engineering, Texas A&M University, College Station, TX 77843-3123, USA
3. School of Chemical, Biological and Materials Engineering, The University of Oklahoma, Norman, OK 73019, USA

Abstract

Magnetic nanoparticle structures have been examined as potential carrier vehicles and substrates in a wide range of applications where they undergo mechanical, chemical and/or thermal manipulation to allow for their modification, conjugation and transport. For safe and effective use, it is imperative to not only measure the initial physicochemical and structural properties of nanomaterials, but also identify and quantify any property changes related to a loss of chemical and/or physical integrity during processing and usage conditions. In this study an assessment of iron oxide magnetic nanoparticle thermal stability using modulated differential scanning calorimetry (mDSC) and a controlled-heating system is conducted on two types of iron oxide nanoparticles: maghemite (Fe_2O_3; 500 nm) with silanol surface functional groups and magnetite (Fe_3O_4; 200 nm) with primary amine terminated alkoxysilane surface functional groups. Modulated differential scanning calorimetry (mDSC) results revealed an endothermic peak at 388 K for both types of nanoparticles indicating possible molecular rearrangement within the structure. To confirm this result, iron oxide nanoparticles were heated while in aqueous suspensions at discrete temperatures ranges from 303 to 403 K. Calorimetry, FT-IR spectroscopy, and dynamic light scattering measurements were used to examine changes in the chemical and physical stability of the suspensions. Morphological characteristics were evaluated using optical microscopy, transmission electron microscopy, and atomic force microscopy. Results showed that

1

*Authors for correspondence: evasquez1@udayton.edu; keisha.walters@ou.edu

the chemical and morphological structure of the nanocomposite is critical in determining the thermal performance of the iron oxide nanoparticles. Amine-terminated silane functionalized magnetite nanoparticles were highly susceptible to morphological and surface-chemistry changes starting at ca. 353 K. Conversely, silanol functionalized maghemite nanoparticles were shown to be stable in terms of morphology and chemical structure up to 403 K. Micrographs demonstrated variations in magnetic domains distribution after exposing the nanoparticles to thermal treatments, confirming the results obtained through mDSC and FT-IR measurements.

1. Introduction

Magnetic nanoparticles are used in a wide range of applications, including drug delivery, magnetic hyperthermia, material separations, energy harvesting and storage, and imaging techniques [1-3]. Effectively utilizing magnetic nanoparticles in these applications requires optimal dispersion and stabilization of the nanoparticles in solution. One approach to accomplish magnetic nanoparticle stabilization and dispersion in solution is the use of a core-shell nanostructure where a magnetic core is surrounded by shell components attached via physical adsorption, covalent bonds and/or electrostatic interactions. The shell-forming compounds, also known as capping agents or ligands, include silica, surfactants, fatty acids, lipids, proteins, and/or polymers [3-5]. One type of magnetic nanoparticle system, agreggates of magnetic nanoparticles (also known as mosaic, cluster, colloidal nano-assembly or nanoflower structures) [6], has recently gained attention as a nanoscale platform to increase heat generation (versus single-core magnetic nanoparticles) during magnetic hyperthermia therapy [7], to remove toxic compounds in environmental remediation applications [8], to manipulate cells and achieve site-specific target

2

using *in vitro* or *in vivo* techniques [9, 10], and to serve as potential carriers of molecular imprinted polymers [11].

One major area of research using magnetic nanoparticles is the biomedical and nanomedicine field [12, 13]. For example, magnetic nanoparticles (MNPs) can be used in biomedical imaging as high contrast agents for magnetic resonance imaging [14-16]. In addition to providing improved imaging capabilities, the clustered nature of MNPs can provide an enhanced magnetic moment and higher separation force under the presence of an external magnetic field as compared to the single core magnetic nanoparticles [17]. Depending on their composition and structure, the inherent superparamagnetic properties, along with nanoparticle manipulation and separation under the influence of an external magnetic field, are strong advantages of these systems and are the focus of current studies on the development of MNPs [18-21] .

In the field of nanotechnology, several applications take advantage of the enhanced magnetization and imaging/contrast properties of MNPs. For instance, magnetic hyperthermia treatment is improved by using MNPs due to an increase in the intrinsic loss power of the nanoparticles, which is attributed to disordered spins within the multicore nanoparticle [7]. Similarly, heat generation can be produced in MNPs under an AC magnetic field due to Neél-like relaxation characteristics, leading to implementation in magnetic hyperthermia and sensor development [22]. Likewise, heating performance and heat dissipation can be enhanced by using chain-like magnetic nanoparticle arrangements under the presence of an external magnetic field [23], or by using magnetic nanocubes, instead of spheres, as the core material [24].

Metallic nanomaterials are well-known to enhance the heat transfer rate in a variety of systems, including heat exchangers, pipe flow, and heat pipes [25-29]. Magnetic nanoparticles dispersed in aqueous solutions—traditionally referred to as ferrofluids or nanofluids—have been shown to

enhance the rate of heat transfer. For example, Heidary et al. demonstrated an increase of 76% in the rate of heat transfer when using a ferrofluid at 0.1 nanoparticle volume fraction and a Hartmann number of 30 in a single channel flow [30]. Utilization of ferrofluids as the working fluid in a heat exchanger increased Nusselt number as the magnetic field was increased, and an increase in the overall thermal performance of traditional heat exchangers using various geometries was observed [31]. Numerical simulations also show that single-core magnetic materials, including magnetite, cobalt ferrite, and manganese zinc-ferrite, cause an increase of the average Nusselt number and the Rayleigh number as the nanoparticle volume fraction increases in natural convective transfer flows [32]. Less entropy generation occurs at high volume fraction of nanoparticles and higher Hartmann numbers [33], making nanoparticle thermal stability highly critical to the thermal performance. Although the majority of studies focus on heat transfer enhancement caused by single-core magnetic materials, recent studies suggest that core-shell magnetic nanoparticles with high specific loss power increase the efficiency of magnetic thermal induction [34]. Therefore, there is a need to understand how thermal treatment affects the stability and properties of surface-functionalized magnetic nanoparticles.

To fully capture the potential of MNPs, material properties, stability, and engineering behaviors need to be better understood—especially as related to the synthesis method and surfactant or coating type. Chemical modifications using a silica matrix [29, 35], crosslinking agents [36], zwitterionic ligands [37], or polymersomes encapsulation [20], have been used to produce stable MNPs. Recently, it was demonstrated that surfactant material and mass are key parameters on the preparation of MNPs with high stability and magnetization dispersed in water [21]. Once stable MNPs are synthesized, there are many potential uses of MNPs in technological applications including sensors, drug delivery vehicles, and the aggregation/stability of stimuli-responsive

coated MNPs under different environments including pH, temperature, and solvent quality [38-41]. The significant growth of interest in MNPs combined with the enhanced manipulation and engineering applications over the past few years motivates a better understanding of the MNPs properties.

This study seeks to analyze the effects of thermal treatments on the stability and performance of core-shell magnetic nanoparticles with distinctive shell components. The primary objective of this effort is to present thermal testing methods to evaluate the physicochemical and morphological properties of two types of commercially available MNPs, with silanol and primary amine surface functional groups. This experimental study exposes these nanoparticle structures to a series of controlled thermal treatments and analyzes the resulting impacts on nanoparticle size, morphology, and chemical composition. Thermal characteristics of each MNP were assessed using thermogravimetric analysis (TG) and modulated differential scanning calorimetry (mDSC). Dispersibilities and dispersion stabilities of these magnetic nanostructures—a critical aspect for colloidal suspensions—were evaluated before and after different thermal treatments with dynamic light scattering. Moreover, MNP morphologies were characterized pre- and post-thermal treatment using transmission electron microscopy, atomic force microscopy, and optical microscopy. The impacts of thermal treatment on the magnetic properties of the magnetic nanoparticles were also examined with magnetic force microscopy. Chemical compositions before and after thermal treatments were assessed using FT-IR spectroscopy and related to changes in changes in morphology and thermal properties due to breakdown of the shell structure.

2. Experimental Section

2.1. Materials

Surface-modified MNPs with distinct particle sizes and surface functionalities were used as-received (50 mg/mL suspensions) from Chemicell, GmBH (Germany). Different surface chemical functional groups surrounds aggregates of iron oxide nanoparticles i) with silanol terminal functional for the SiMAG-Silanol samples (500 nm, maghemite (Fe_2O_3)) and ii) with primary amine functional groups on the FluidMAG-Amine samples (200 nm, magnetite (Fe_3O_4)). Throughout this study, the magnetic nanoparticles (MNPs) with terminal silanol function groups will be referred to as SiOH-MNPs. The MNPs with an amine functional group will be referred to NH_2-MNPs. For all dilutions, ultra-pure Type I water (Millipore Q Synergy UV, resistivity of 18.2 MΩ·cm at 298 K) was used.

2.2 Thermal Characterization

2.2.1 Thermogravimetric Analysis (TG). To assess the capping agent stability as a function of temperature, each MNP was dried and then characterized using a TA Instrument Q-600 simultaneous DSC-TG apparatus. Samples were dried for at least 72 h in the TG crucible at room temperature inside a ventilated hood, and a minimum of 5 mg of sample was used for each run. TG experiments were performed from ambient temperature to ~ 1125 K under a constant nitrogen flow of 50 mL/min. The instrument has a balance sensitivity of 0.1 μg and a sensitivity of 0.001 °C for differential thermal analysis. Data analysis was performed using TA Universal Analysis 2000 software.

2.2.2 Modulated Differential Scanning Calorimetry (mDSC). To evaluate any change in the thermal flow analysis—and related phase transitions—due to the thermal treatments, mDSC experiments were performed *in situ*. For mDSC measurements a TA Instrument Q2000 research-grade DSC was used with a temperature accuracy of ± 0.1 °C and a sensitivity of 0.2 μW. The reversing heat flow signal provided by mDSC measurements can indicate variations in heat

6

capacity. Reversing heat flow was calculated by multiplying this constant by the rate of heat flow amplitude divided by the heating rate amplitude. A modulation amplitude and modulation period of 0.5 K and 40 s, respectively, were used throughout the study. Samples were heated from -233.15 K to 433.15 K with a heating rate of 10 K min^{-1} under a nitrogen purge (50 cm^3 min^{-1}). Calibration constants were obtained from running mDSC measurements of sapphire standards. To prepare the samples, MNP suspensions were placed into a DSC pan, sealed with a hermetic lid, and then analyzed. A minimum mass of 3 mg of the dried MNPs suspension was used for DSC characterization of each sample.

2.2.3 Thermal Treatments Using a Heating Apparatus

To examine thermal stability under constant heating and mixing, MNPs in 1 mg cm^{-3} suspensions were submitted to heating treatments at different temperatures using the apparatus shown in **Fig. S1 (ESM 1)**. During heating, the nanoparticle solutions were not exposed to oxygen, and a nitrogen purge was maintained throughout the experiment to avoid any potential oxidation. In order to characterize the physicochemical and morphological conditions of the samples exposed at different temperatures, small aliquots were collected at different temperature conditions: 303.15 K, 353.15 K, 373.15 K, 393.15 K, and 403.15 K (heating element set point temperatures). Temperature set points in each heating cycle were monitored throughout the process by using a digital temperature controller (CG-15001 OptiChem®, Chemglass). The temperature controller provides 1500 W of power and a ± 1.0 °C control. Sample aliquots were collected from the reflux apparatus at each temperature after a one-minute equilibrium hold time. Then, samples were allowed to cool to room temperature (~1 h) under ambient conditions prior to analysis and characterization.

2.3 Morphology, Particle Size, and Magnetic Characterization

Morphological characterization of the MNPs was performed using transmission electron microscopy, atomic force microscopy, and optical microscopy. A JEOL 2100 TEM operated at 200 kV was used to obtain micrographs before and after thermal treatments. A resolution as a high as 0.19 nm can be achieved with this instrument. Untreated and treated samples were prepared by placing a sample drop of the colloidal suspension ($\sim$ 1 mg cm^{-3}) on a carbon Formvar Cu grid (300 mesh; Electron Microscopy Science). The solvent was allowed to evaporate inside a ventilated hood. Atomic- and magnetic- force microscopy data were collected with a Dimension Icon instrument (Bruker) in tapping mode using a Co-Cr coated tip on a silicon cantilever (MESP, Bruker). The instrument has x-y position noise of less than 0.15 nm and Z-sensor noise level of 35 pm RMS bandwidth. The probe was magnetized for 30 seconds using an external magnet prior to measurement, and a lift of 100 nm was used for data collection. Optical microscopy images were obtained using the Dimension Icon microscope camera (5 megapixels). Dynamic light scattering was used to measure the hydrodynamic diameter of the particles and particle size distribution in solution before and after thermal treatment (Section 2.2.3). Variations in nanoparticle hydrodynamic diameter after thermal treatments can be attributed to nanoparticle aggregation or break-down from the as-received samples. A Brookhaven ZetaPALS instrument (Brookhaven Instruments Corporation; BIC) with a 90° detector and a HeNe laser at a 659 nm wavelength was used to collect the DLS data. A minimum concentration of 2 ppm is required for data collection. The precision of the instrument is $\pm$ 1%of the reading. Data were collected at ambient temperature ($\sim$ 295 K) and a minimum of five measurements were collected per sample. Average results are presented.

2.4 Chemical Characterization using ATR-FTIR

Magnetic nanoparticles were characterized using attenuated total reflection FTIR (ATR-FTIR) with a Nicolet 6700 FTIR spectrophotometer (Thermo Electron Corporation Inc.) and Miracle-ATR[TM] accessory (PIKE Technologies Inc.). The FTIR instrument is equipped with a He-Ne laser, MCT-A* detector, and KBr beamsplitter, and has a wavenumber precision of 1cm. The Miracle-ATR accessory has a diamond crystal with ZnSe filter (1.8 mm diameter) and a 45° angle of incidence, with an accuracy of $\pm$ 0.5%. ATR-FTIR spectra of sample solutions before and after thermal treatments were collected via dropwise solution deposition onto the ATR crystal followed by solvent evaporation at room temperature, leaving a thin film of the sample on the crystal surface. Omnic software (v8.1.10; Thermo Electron Corporation Inc.) was used for data collection and analysis with a minimum of 256 scans collected for each sample.

3. Results and Discussion

3.1. Thermal Characterization of Magnetic Nanoparticles (MNPs)

Thermogravimetric analysis (TG) and differential thermogravimetric (DTG) methods can provide insight into the thermal stability of polymers or ligands used to stabilize nanoscale materials [45, 46]. For example, MgO and SiO_2 have both been used on the surface of single core nanoparticles as protective layers to prevent nanoparticle sintering at high temperatures, enabling the production of monodisperse and thermally stable nanoparticles [47, 48]. Similarly, multicore magnetic nanoparticles have been stabilized using polymers [10, 15], silanization techniques [49], and natural fatty acids [50]. However, little is known about the stability of these protective layers as a function of temperature or thermal treatments. Reorganization, phase transformation, chemical

9

degradation and/or release of these protective layers/shells on the nanoparticle surface is likely to lead to particle aggregation.

Figure **1** shows TG scans from ambient temperature to ~ 1125 K of the amine and silanol-functionalized MNPs examined in this study. Both commercial MNP suspensions were dried under ambient temperature conditions inside a ventilated hood for at least 72 h prior to TG analysis. Below 373 K, the DTG curves for both NH_2-MNPs (Fig. **1A**) and SiOH-MNPs (Fig. **1B**) exhibited peaks indicating the release of trapped water from the particles. SiOH-MNPs showed a slower release of water compared to NH_2-MNPs, perhaps due to the less polar nature of the amine, nitrogen being less electronegative than oxygen and the weaker N-H dipole resulting in less water being bonded, and a quicker release of the bound water. Dehydration of the nanoparticles accounted for ~1.5% and ~3.8% mass loss in NH_2-MNP and SiOH-MNP, respectively. Above 373 K, a steady mass loss was observed for NH_2-MNPs until a temperature of 883 K was reached (Fig. **1A**), where a sharp decrease in mass of ~1.0% was observed. Between 883 K and 1125 K, the sample mass for NH_2-MNPs remained constant. For SiOH-MNP, the DTG analysis reveals a small but sharp change in mass at approximately 473 K that is not observed in the NH_2-MNPs. However, both samples showed similar thermal profiles and overall mass loss with over 94% of the initial sample mass remaining between 473 to 873 K. The gradual mass loss noted from 373-873 K could be due to decomposition of the surface stabilizers. Both NH_2-MNP and SiOH-MNP are comprised of cubic structures—Fe_3O_4 and Fe_2O_3, respectively—that are prone to a phase transition to α-Fe_2O_3 (hematite) in the range of 723 – 923 K [51]. When kept intact, a refractory shell matrix such as a silica shell can prevent the irreversible transformation into hematite [52]. Significant mass losses noted at 473 K for SiOH-MNP and ca. 873 K for SiOH-MNP and NH_2-MNP. In the NH_2-MNP structures, one strong mass loss peak is found at

ca. 873 K and it is attributed to a hematite phase transition. For SiOH-MNP, the mass changes

observed are much more slight and may be due to water release from the silica shell due to

condensation reaction of the alkoxysilane [53], which in theory could then be followed by the

oxidation of maghemite to hematite (at ~873 K). The proposed transformation of the nanoparticle

structures followed by a phase transition to hematite is also supported by the sharp DTG peaks

present. It should be noted that although there is a maximum 6% mass loss as temperature is

increased (T_{max} = 1125 K), this result is comparable to other reported value for iron oxide

nanoparticles with silica shells [54]. Here, using TG and DTG thermal analysis, we indicate that

the iron oxide nanoparticles within the MNP matrix are stable up to a temperature of 1125 K, and

further analysis is performed by using additional experimental techniques.
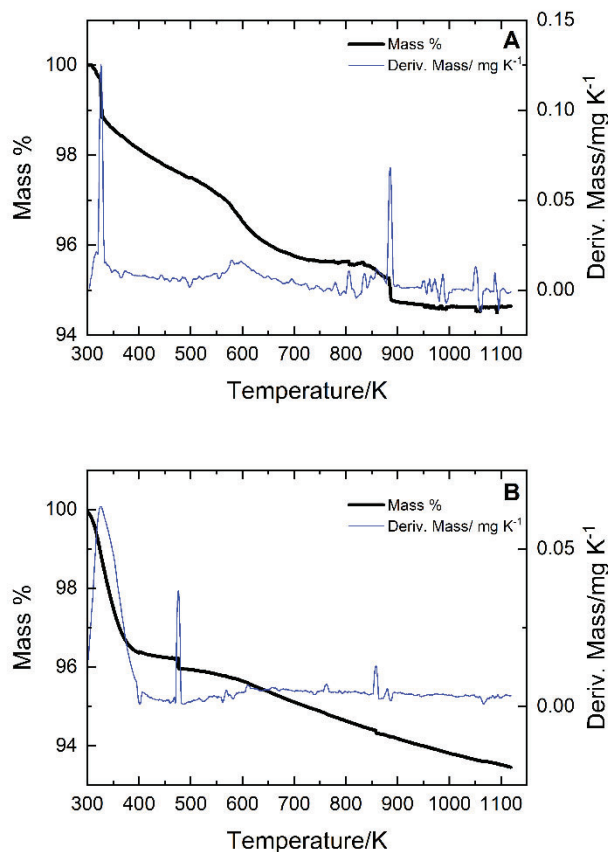
Fig. 1 TG and DTG analyses from ambient temperature to 1125 K of (A) NH_2-MNPs and (B) SiOH-MNPs samples reveal evidence of partial silica shell decomposition with potential oxidation of released nanoparticle to hematite.

TG and DTG can only provide insight into the break down and removal of components from a sample. In order to investigate thermal phase transitions of these multicomponent nanoparticles, modulated DSC (mDSC) experiments were performed on the MNPs while in aqueous suspension. mDSC is a unique characterization tool as it allows for the measurement of weak transitions and complex thermal processes that cannot be observed with traditional DSC [55]. For example, structural changes and phase behavior of poly(ethylene oxide) have been studied using mDSC [56]. Similarly, mDSC of poly(methyl methacrylate) adsorbed on silica determined the bonded amounts of polymer on the substrate [57].

Using mDSC, phase transitions and thermal events were examined for both MNP samples (Figure **2**). The mDSC scans for NH_2-MNPs (Fig. **2A**) display a strong endothermic peak at 388 K for both heating cycles and the cooling cycle. As shown in Fig. **2B**, endothermic peaks were also observed for SiOH-MNP, although they are weaker than those observed for NH_2-MNPs. Also, no peaks were observed for the cooling cycle of SiOH-MNPs, indicating possible differences in microstructural rearrangements between both iron oxide nanostructures. The presence of endothermic peaks in the reversing heat flow mDSC signal correspond to transitions related to molecular mobility in polymers [58], structural rearrangements into clusters [59], and/or order-disorder measures of molecular level reordering within clusters [60]. The observed endothermic peak at 388 K for both MNPs is attributable to molecular rearrangement within the MNP cluster related to a possible release of individual iron oxide cores from the aggregated MNP structure. Above this transition temperature at 388 K, no endothermic or exothermic peaks were observed for either the heating or cooling traces.
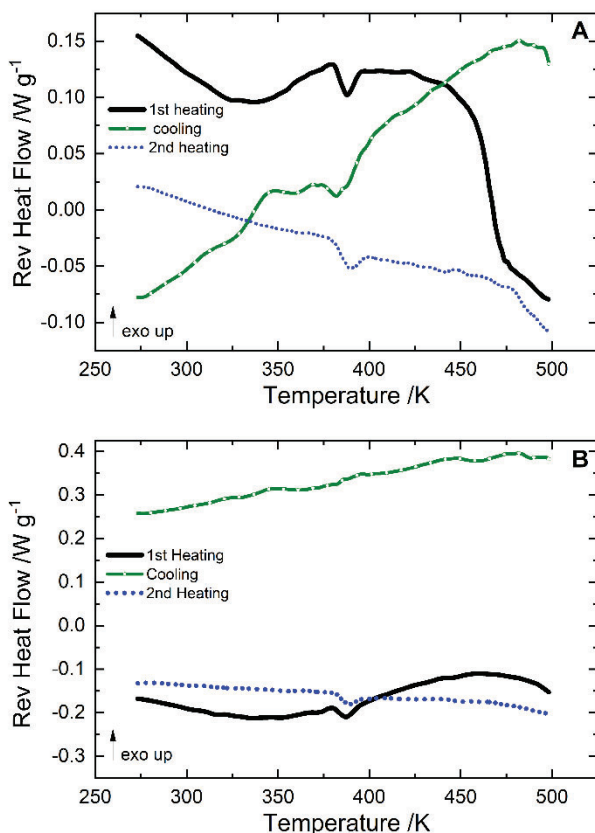
Fig. 2 Modulated DSC results for (A) NH$_2$-MNPs and (B) SiOH-MNPs from 273 to 498 K. Endothermic peaks observed at 388 K are stronger for the amine-functionalized nanoparticles as compared to the silanol-functionalized nanoparticles.

Ultimately TG and mDSC results for the MNPs suggest a magnetic nanoparticle phase change and a possible rearrangement within these coated magnetic nanoparticles at temperatures above 388 K. To confirm the performance of MNP structures to thermal stresses and to obtain a correlation between thermal treatments and possible morphology and chemical changes, an additional controlled temperature treatment was performed on each MNP type. Morphological analyses and chemical structure characterization were also conducted to confirm changes in the MNP structures observed with calorimetry measurements.

3.2 In situ Thermal Treatment of Magnetic Nanoparticles: Effects on Nanoparticle Size,

Stability, and Morphology

According to the observed *in situ* mDSC endothermic peak transitions for both MNPs, the integrity and stability of the MNP structure in solution are affected by exposure to elevated temperatures. To investigate thermal stability further, dynamic light scattering was used to measure the hydrodynamic diameter of particles in solution after they were heated to a given testing temperature in the reflux apparatus described in section 2.2.3. Hydrodynamic particle size distributions in suspension before and after thermal treatment for both MNPs across several aliquot tests are shown comparatively in Figure **3**. For the SiOH-MNP samples, exposure to elevated temperature did not cause any significant change in hydrodynamic diameter. A mean diameter of ~600 nm was measured at all the temperature conditions tested (298, 353, 393, and 403 K), and this diameter is close in value to vendor-reported diameter (~500 nm). The DLS data demonstrate SiOH-MNP is a thermally stable structure. Therefore, the slight endothermic transition noted for SiOH-MNP using mDSC must not be related to particle aggregation or cluster formation but rather could be due to conformational rearrangement of the nanoparticles within the shell.

Conversely, NH_2-MNP showed variations in hydrodynamic diameter as temperature increased (Fig. **3**). At 298 K, NH_2-MNPs in suspension had a diameter ~225 nm, which is close in value to the ~200 nm vendor-reported diameter. The hydrodynamic diameter for NH_2-MNP increased significantly as a function of temperature, up to an average value of ~2 µm when a reflux temperature of 403 K was reached. This increase in hydrodynamic diameter is attributed to particle aggregation. While the mDSC data showed a thermal transition temperature at ca. 388 K, hydrodynamic diameter changes showed NH_2-MNP is unstable in suspension at even lower

temperatures (~373 K). These results support the structural changes indicated by TG and DTG for NH_2-MNPs: a major change in structure that leads to aggregation of the nanoparticles. It is proposed that thermal treatments results in aggregation of the iron oxides nanoparticles previously located within the amine-coated shell matrix leading to large-scale particulates. As a result, abrupt and large differences in the hydrodynamic NH_2-MNPs diameters were observed. To confirm these results, additional morphological analyses were performed as described next.
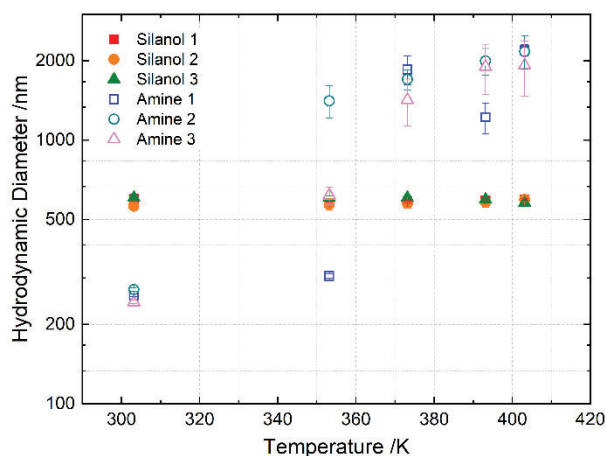
**Fig. 3** Hydrodynamic diameters measured after reflux at a given temperature for silanol-functionalized magnetic nanoparticles (SiOH-MNPs, closed symbols) and amine-functionalized magnetic nanoparticles (NH_2-MNPs, open symbols); these dynamic light scattering data reveal NH_2-MNP are thermally unstable.

In addition to the structural analysis of the hydrodynamic particle size changes, optical microscopy, transmission electron microscopy, and atomic- magnetic- force microscopy were used to image the dried MNP samples prior and before thermal treatments. With these microscopy techniques, the effects of thermal treatment on the iron oxide nanoparticles morphology and subsequent structural changes were assessed demonstrating morphological and visual modifications of SiOH-MNPs suspensions after exposure to elevated thermal treatments and high shear conditions (Fig. **S2**). The clustered nature and morphological characteristics of the nanoparticles used in this study have been validated by other research groups [42-44]. Here, this

work seeks to obtain a better understanding between thermal treatments and structural integrity of the multi-core iron oxide nanoparticles.

As shown previously [61], amine-functionalized multi-core magnetic nanoparticles have an irregular, non-rounded surface structure. In the present study, similar surface features were observed for the as-received NH_2-MNP (Fig. **4A**). However, after a thermal treatment, aggregates were observed in the NH_2-MNP samples, likely due to aggregated silica shells or uncoated iron oxide nanoparticles. The sizes of these structures are comparable to the hydrodynamic diameter largest particulates (~2 μm) for thermally-treated NH_2-MNPs (Fig. **4B**). In addition, aggregated magnetic nanoparticles (Fig. **4C**) and also dispersed primary particle magnetic nanoparticles—those from the interior/core of the nanostructures—were observed (Fig. **4D**). This combination of features results from the possible rearrangement of the shell structure leading to unstable surfaces, and the release of the small primary iron oxide nanoparticles that were previously part of the core-shell structure. These micrographs of the released and aggregated particles show that the NH_2-MNPs are thermally unstable and corroborates the MNP aggregation indicated by thermal and dynamic light scattering characterization methods.

16
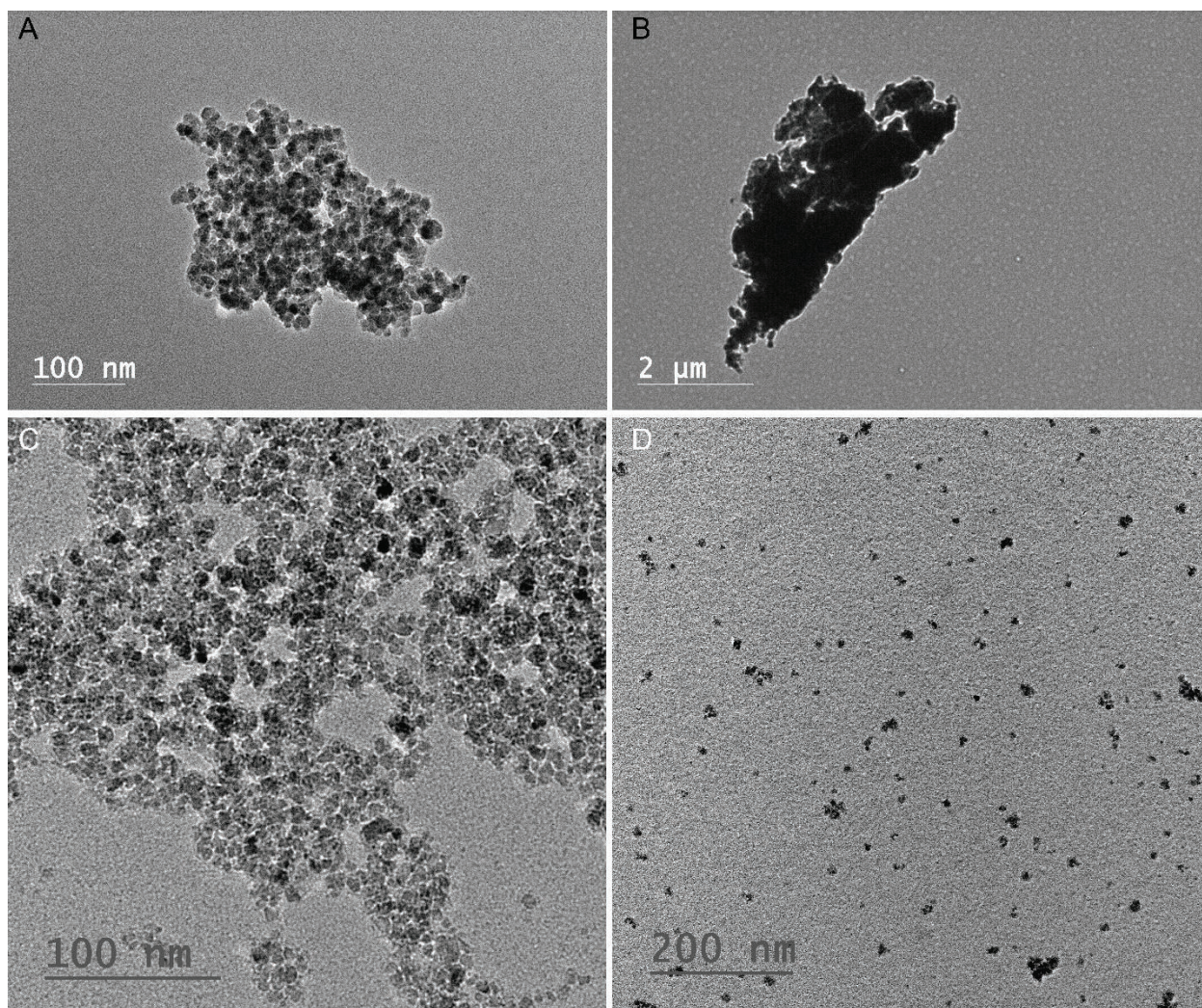
Fig. 4 TEM images of NH$_2$-MNPs, (A) as-received and (B-D) after thermal treatment. NH$_2$-MNPs samples submitted to thermal treatment resulted in released and aggregated pieces of the shell (B), large-scale aggregations of iron oxide nanoparticles (C), and residual iron oxide clusters released from the MNP core (D).

Unlike NH$_2$-MNP, mDSC and dynamic light scattering characterization results for SiOH-MNP indicate these sample to be thermally stable. Micrographs of the SiOH-MNP prior to (Fig. **5A**) and after (Fig. **5B**) sample heating described in this work reveal that these samples maintain their structure over the 303 – 403 K temperature range tested. In terms of morphology, SiOH-MNP possesses a well-defined spherical shape—as shown in Fig. 5 and by Chemicell [62]—which contrasts significantly with the structural changes observed for NH$_2$-MNP [63]. The stark structural differences between these two types of MNPs may indicate a different MNP fabrication method for

17

each nanoparticle type. Ultimately, however, the structural and resultant phase transitions related to the protective shell depend on the methods utilized for synthesis of each MNP [64].

The SiOH-MNP sample has a round shell encapsulating the core primary nanoparticles (Fig. **5A**) while the NH$_2$-MNP sample looks to only have at most only a small amount of surface functionalization (Fig. **4A**) and so a complete 'shell' is not formed around the aggregated iron oxide nanoparticles. The morphology of the aggregated iron oxide nanoparticle structure for the amine functionalized nanoparticles has been documented in previous studies [65, 42]. Only after heating the SiOH-MNP samples at the highest temperatures tested in this study (ca. 403 K), were any aggregates observed (Fig. **S3**), and there was only a few. These aggregates were exceptions, with the vast majority of the thermally treated SiOH-MNP sample appearing as shown in **Fig. 5B**. These results corroborate the findings from thermal and dynamic light scattering characterization showing the SiOH-MNPs samples maintained their structure during thermal treatment without widespread shell deformation or aggregation—unlike the amine-functionalized MNPs. Atomic- and magnetic-force microscopy results for a SiOH-MNP sample set also provide evidence that the morphological structure for SiOH-MNP is not impacted by the thermal treatments in this study (**Fig. S4**). However, the thermally treated SiOH-MNP samples show loss of magnetic properties, as observed in the magnetic phase images, suggesting that individual magnetic cores leaked from the shell structure (Figs. **S4C and S4F**).
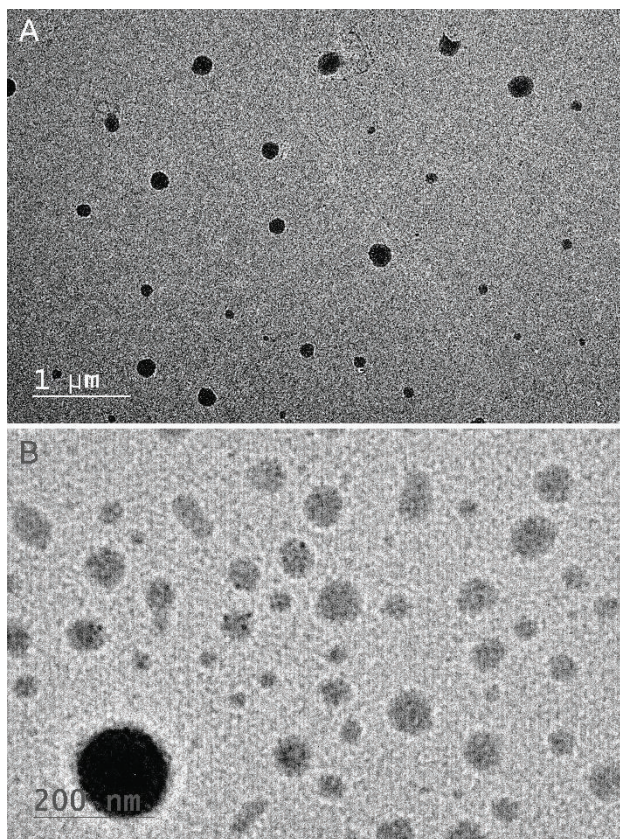
Fig. 5 TEM images of SiOH-MNP prior to thermal treatment (A) and after thermal treatment (B) revealed few morphological and structural changes.

3.3 Magnetic Nanoparticle (MNP) Chemical Structure Characterization

In addition to analysis of the MNP thermal properties, hydrodynamic diameter, size distributions, magnetic properties, and morphologies pre- and post-thermal treatment, potential chemical transformations related to thermal treatment were also examined. ATR-FTIR spectroscopy was used to determine functional groups present in the MNPs before and after the reflux thermal treatments were performed. FTIR spectra for the silanol coated magnetic nanoparticles (SiOH-MNP) samples before and after thermal treatment are shown in Fig. **6**.
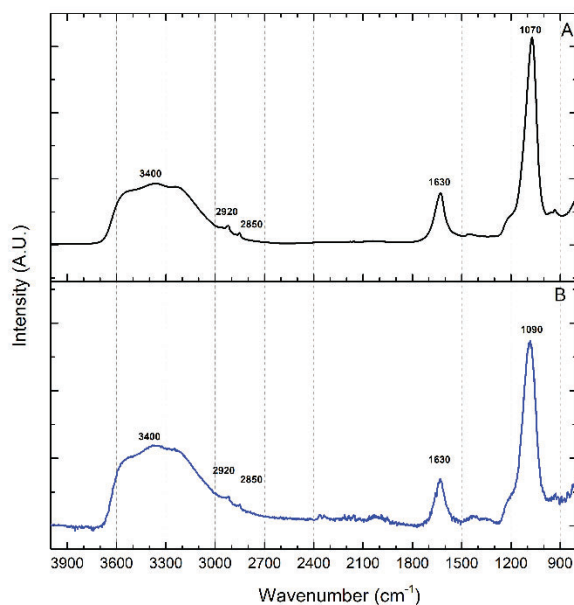
Fig. 6 ATR-FTIR spectra of SiOH-MNPs before (A) and after (B) thermal treatment support nanoparticle leakage as a peak shift is observed from 1070 to 1090 cm^{-1}corresponding to the Si-O bond.

A broad absorption band at 3400 cm^{-1} confirms the presence of stretching vibrations from the −OH groups present on the surface of the MNPs. An additional peak located at 1630 cm^{-1} suggest that −OH groups are coating the surface of the magnetic nanoparticles as reported elsewhere [66]. The peak at ~1070 cm^{-1} confirms the presence of Si−O stretching vibrations, which are expected to be present in the structure of the silanol compound surrounding a core-shell magnetic nanoparticle structure [67]. In addition, the broad peak at 3400 cm^{-1} has been attributed to hydrogen-bonded silanol and absorbed water on the surface of the magnetic nanoparticles [68]. Lastly, the two bands at 1920 cm^{-1} and 2850 cm^{-1} confirm the presence of C−H asymmetric and symmetric stretching vibrations, respectively. Fig. **6B** displays the FT-IR spectrum of the silanol magnetic nanoparticles after thermal processing techniques described in the experimental section. Infrared absorptions bands were not highly affected by the heat treatment suggesting no major chemical changes and a stable SiOH-MNPs. However, after the thermal treatment, a peak shift in the Si-O peak maximum was observed from 1070 to 1090 cm^{-1}. Similar transitions have been

assigned to asymmetric stretching motion of oxygen in various silicon-oxygen bands under annealing conditions [69]. In this study, the IR band shift is assigned to a magnetic nanoparticle leakage from the shell caused by a possible rearrangement of the silanol coating, which confirms the mDSC results and the magnetic force microscopy imaging.

NH_2-MNPs were also submitted to multiple heating treatments, and ATR-FTIR spectroscopy was conducted to evaluate changes in molecular structure. **Fig. 7A** shows the as-received NH_2-MNPs IR spectrum, which had been previously analyzed using ATR-FTIR and peak assignments described in detail by the authors [61]. The peaks critical for identifying the chemical composition of the MNPs before and after thermal treatment are presented. The presence of amine-terminated silane on the NH_2-MNP surface is supported by the presence of a broad peak corresponding to primary amine N-H stretching vibrations (3360 cm^{-1}), a peak at ca. 1640 cm^{-1} for the $-NH_2$ and/or $N-H$ deformation/stretching vibrations, and an absorption band at 1010 cm^{-1} which can be attributed to the $Si-O$ stretching vibrations and/or $N-C-N$ symmetric stretching [70]. Additionally, the small 1540 cm^{-1} peak corresponds to NH_2 scissor vibrations, demonstrating an amine end-functionalized group on the MNP surface [71]. Both, peaks present at 1540 cm^{-1} and at 1010 cm^{-1} wavenumber, confirm the presence of amine functionalized groups on the outer surface of the core-shell structure prior thermal treatments.
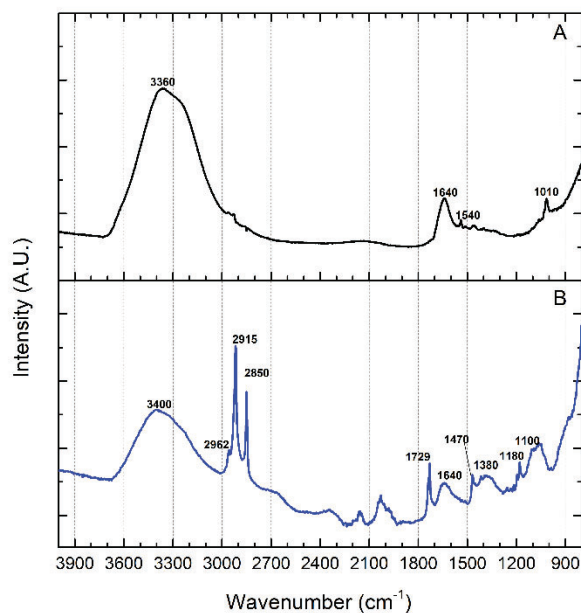
Fig. 7 ATR-FTIR spectra for NH_2-MNP before (A) and after (B) thermal treatment. The presence of additional absorption bands after heating supports particle aggregation due to thermal stress.

After heating at temperatures above the boiling point of the solvent, NH_2-MNP samples demonstrated peak shifts and significantly stronger additional peak absorbances were observed (Fig. **7B**). Note, however, that this result was not observed for the SiOH-MNP samples. A broader absorption band was observed at ~3400 cm^{-1} after the thermal treatment. However, in this region $-NH_2$ groups and O$-$H stretching vibration can overlap [72]. After heating, a new peak at 1729 cm^{-1} was observed for the NH_2-MNP sample, and it can be attributed to C=O groups that are unbounded due to thermal decomposition of the nanostructure shell [73]. Similarly the peaks at 1470 cm^{-1} and 1380 cm^{-1}, for CH_2 and CH_3 bending vibrations, were not observed in the untreated sample (Fig. **7A**) but were present after thermal treatment. Additionally, the strong intensity of asymmetric and symmetric stretching vibrations for C$-$H bands (2962 cm^{-1}, 2915 cm^{-1}, and 2850 cm^{-1}) observed in the post-treated sample suggest a release of the alkyl groups from the shell matrix [74]. The presence of the 1180 cm^{-1} peak post-heating (Fig. **7B**) is likely related to the exposure of alkoxysilanes after thermal treatments, as this absorbance band is attributable

to CH_3 rocking in alkoxysilanes [74, 75]. The appearance of multiple new absorbance bands after thermal treatment confirms release or aggregation of the amino-functionalized alkoxysilane shell for NH_2-MNP. A broad peak at 1100 cm^{-1} is assigned to the Si-O molecular bond, confirming the presence of the silane structure.

FT-IR results confirmed the thermal instability observed for NH_2-MNP with mDSC, and morphological characterization analyses. The significant differences observed in thermal stability of the two type of MNP—amine and silanol functionalized—are likely due to differences in the methods used to produce the two functionalized shells around the magnetic nanoparticle cores. In this study, however, the authors demonstrate that mDSC measurements can be used to predict nanoparticles self-arrangements or organization within a shell structure, which could ultimately be used as a simple tool to predict nanoparticle stability as a function of temperature. Here a combination of morphological and physicochemical studies were used to confirm the observed changes on mDSC measurements.

4. Conclusions

Stability of magnetic nanoparticles is a key element for their use in a wide range of applications. This study presents thermal, morphological, and physicochemical examinations for two types of multi-core magnetic nanoparticles made up of a silica-shell and a core comprised of multiple iron oxide nanoparticles—before and after thermal treatment over the 303-403 K temperature range. mDSC and TG/DTG analyses were also used as experimental techniques to evaluate nanoparticles thermal stability, resulting in the presence of endothermic peaks which are attributed to a rearrangement of the iron oxide nanoparticles within the shell, and confirmed with other experimental techniques. Further, treatment of both MNPs under a controlled heating

system resulted in nanoparticle aggregation for NH_2-MNP samples, and a release of the iron oxide nanoparticles from the shell for the SiOH-MNP samples. Amine-functionalized MNP were shown to aggregate even at moderate temperatures (353 K), which could be due to incomplete coverage and/or low-density of the amine-functionalized alkoxysilane shell coating, with a subsequent aggregation of the unstable nanoparticles into large, micron-scale structures. Conversely, silanol-functionalized MNP were shown to be much more stable, as these showed only limited nanoparticle leakage from the core up at the highest temperature tested in this study, 403 K. The significant differences in the amine- and silanol-functionalized MNP sample thermal stabilities can be attributed to the type of encapsulation method utilized to fabricate these two types of MNPs; however, future studies analyzing the link between synthesis routes and thermal stability with mDSC and the techniques presented in this study are suggested.

A better understanding of the thermal, chemical and mechanical stability of iron oxide nanocomposites is critical, as these structures are targeted in applications where a lack of structural integrity could cause irreversible damage to human health and the environment. The findings presented in this work serve as a foundation for thermal stability testing methods and the impact of shell chemistries on thermal stability and can be extended to other nanostructures to help direct structural and chemical design and ensure adequate thermal performance.

Conflicts of interest

There are no conflicts of interest to declare.

Acknowledgements

† **Electronic Supplementary Information (ESM) available:** Supplemental information and data for this document is available online.

References

1. Latham AH, Williams ME. Controlling transport and chemical functionality of magnetic nanoparticles. Accounts Chem Res. 2008;41(3):411-20. https://doi.org/10.1021/ar700183b
2. Monroe JG, Vasquez ES, Aspin ZS, Walters KB, Berg MJ, Thompson SM. Electromagnetic induction by ferrofluid in an oscillating heat pipe. Appl Phys Lett. 2015;106. https://doi.org/10.1063/1.4923400
3. Woo E, Ponvel KM, Ahn I-S, Lee C-H. Synthesis of magnetic/silica nanoparticles with a core of magnetic clusters and their application for the immobilization of His-tagged enzymes. Journal of Materials Chemistry. 2010;20(8):1511-5. https://doi.org/10.1039/B918682D
4. Bohara RA, Thorat ND, Pawar SH. Role of functionalization: strategies to explore potential nano-bio applications of magnetic nanoparticles. RSC advances. 2016;6(50):43989-4012. https://doi.org/10.1039/C6RA02129H
5. Rabbani Y, Hajinajaf N, Tavakoli O. An experimental study on stability and rheological properties of magnetorheological fluid using iron nanoparticle core–shell structured by cellulose. Journal of Thermal Analysis and Calorimetry. 2019;135(3):1687-97. https://doi.org/10.1007/s10973-018-7538-7
6. Bogren S, Fornara A, Ludwig F, Del Puerto Morales M, Steinhoff U, Hansen MF et al. Classification of Magnetic Nanoparticle Systems--Synthesis, Standardization and Analysis Methods in the NanoMag Project. International Journal of Molecular Sciences. 2015;16(9):20308-25. https://doi.org/10.3390/ijms160920308
7. Bender P, Fock J, Frandsen C, Hansen MF, Balceris C, Ludwig F et al. Relating Magnetic Properties and High Hyperthermia Performance of Iron Oxide Nanoflowers. The Journal of Physical Chemistry C. 2018;122(5):3068-77. https://doi.org/10.1021/acs.jpcc.7b11255
8. Wells J, Kazakova O, Posth O, Steinhoff U, Petronis S, Bogart LK et al. Standardisation of magnetic nanoparticles in liquid suspension. Journal of Physics D: Applied Physics. 2017;50(38):383003. https://doi.org/10.1088/1361-6463/aa7fa5
9. Marcus M, Karni M, Baranes K, Levy I, Alon N, Margel S et al. Iron oxide nanoparticles for neuronal cell applications: uptake study and magnetic manipulations. Journal of Nanobiotechnology 2016;14(1):37. https://doi.org/10.1186/s12951-016-0190-0
10. Eberbeck D, Dennis CL, Huls NF, Krycka KL, Gruttner C, Westphal F. Multicore Magnetic Nanoparticles for Magnetic Particle Imaging. IEEE Transactions on Magnetics 2013;49(1):269-74. https://doi.org/10.1109/TMAG.2012.2226438
11. Urraca JL, Cortés-Llanos B, Aroca C, Presa Pdl, Pérez L, Moreno-Bondi MC. Magnetic Field-Induced Polymerization of Molecularly Imprinted Polymers. The Journal of Physical Chemistry C. 2018;122(18):10189-96. https://doi.org/10.1021/acs.jpcc.7b12804
12. Bhandari S, Khandelia R, Pan UN, Chattopadhyay A. Surface Complexation-Based Biocompatible Magnetofluorescent Nanoprobe for Targeted Cellular Imaging. ACS Applied Materials & Interfaces. 2015;7(32):17552-7. https://doi.org/10.1021/acsami.5b04022
13. Pan UN, Sanpui P, Paul A, Chattopadhyay A. Surface-Complexed Zinc Ferrite Magnetofluorescent Nanoparticles for Killing Cancer Cells and Single-Particle-Level

Cellular Imaging. ACS Applied Nano Materials. 2018;1(6):2496-502. https://doi:10.1021/acsanm.8b00545

14. Jirák Z, Kuličková J, Herynek V, Maryško M, Koktan J, Kaman O. Titania-coated manganite nanoparticles: Synthesis of the shell, characterization and MRI propertie. J Magn Magn Mater. 2017;427:245-50. https://doi.org/10.1016/J.JMMM.2016.10.097

15. Balasubramaniam S, Kayandan S, Lin YN, Kelly DF, House MJ, Woodward RC, St. Pierre T.G., Riffle, J.S., Davis, R.M. Toward design of magnetic nanoparticle clusters stabilized by biocompatible diblock copolymers for T 2-weighted MRI contrast. Langmuir. 2014;30(6):1580-7. https://doi.org/10.1021/la403591z

16. Ao L, Wang B, Liu P, Huang L, Yue C, Gao D, Wu C, Su W. A folate-integrated magnetic polymer micelle for MRI and dual targeted drug delivery. Nanoscale. 2014; 6, 10710-10716. https://doi.org/10.1039/C4NR02484B

17. Zoppellaro G, Kolokithas-Ntoukas A, Polakova K, Tucek J, Zboril R, Loudos G, Fragogeorgi, E, Diwoky C, Tomankova K, Avgoustakis K, Kouzoudis D, Bakandritsos A. Theranostics of epitaxially condensed colloidal nanocrystal clusters, through a soft biomineralization route. Chem Mater. 2014; 26(6): 2062-74. https://doi.org/10.1021/cm404053v

18. Javed Y, Lartigue L, Hugounenq P, Vuong QL, Gossuin Y, Bazzi R, Wilhelm C., Ricolleau C, Gazeau F, Alloyeau D. Biodegradation Mechanisms of Iron Oxide Monocrystalline Nanoflowers and Tunable Shield Effect of Gold Coating. Small. 2014; 10(16): 3325-3337. https://doi.org/10.1002/smll.201400281

19. Kostopoulou A, Brintakis K, Fragogeorgi E, Anthousi A, Manna L, Begin-Colin S, Billotey C, Ranella A, Loudos G, Athanassakis I, Lappas A. Iron Oxide Colloidal Nanoclusters as Theranostic Vehicles and Their Interactions at the Cellular Level. Nanomaterials. 2018;8(5):315. https://doi.org/10.3390/nano8050315

20. Hickey RJ, Koski J, Meng X, Riggleman RA, Zhang P, Park SJ. Size-controlled self-assembly of superparamagnetic polymersomes. ACS Nano. 2014;8(1):495-502. https://doi.org/10.1021/nn405012h

21. Abadeh A, Passandideh-Fard M, Maghrebi MJ, Mohammadi M. Stability and magnetization of Fe3O4/water nanofluid preparation characteristics using Taguchi method. Journal of Thermal Analysis and Calorimetry. 2019;135(2):1323-34. https://doi.org/10.1007/s10973-018-7662-4.

22. Lai J-J, Lai W-R, Chen C-Y, Chen S-W, Chiang C-L. Multifunctional magnetic plasmonic nanoparticles for applications of magnetic/photo-thermal hyperthermia and surface enhanced Raman spectroscopy. J Magn Magn Mater. 2013; 331: 204-207. https://doi.org/10.1016/j.jmmm.2012.11.051

23. Serantes D, Simeonidis K, Angelakeris M, Chubykalo-Fesenko O, Marciello M, Morales MdP, Baldomir D, Martinez-Boubeta C.Multiplying Magnetic Hyperthermia Response by Nanoparticle Assembling. The Journal of Physical Chemistry C. 2014; 118(11): 5927-5934. https://doi.org/10.1021/jp410717m

24. Martinez-Boubeta C, Simeonidis K, Makridis A, Angelakeris M, Iglesias O, Guardia P et al. Learning from Nature to Improve the Heat Generation of Iron-Oxide Nanoparticles for Magnetic Hyperthermia Applications. Sci Rep. 2013;3. https://doi.org/10.1038/srep01652

25. Nakhchi ME, Esfahani JA. Cu-water nanofluid flow and heat transfer in a heat exchanger tube equipped with cross-cut twisted tape. Powder Technol. 2018; 339: 985-994. https://doi.org/10.1016/j.powtec.2018.08.087

26. Nakhchi ME, Esfahani JA. Entropy generation of turbulent Cu–water nanofluid flow in a heat exchanger tube fitted with perforated conical rings. Journal of Thermal Analysis and Calorimetry. 2019;138(2):1423-36. https://doi.org/10.1007/s10973-019-08169-w

27. Nakhchi ME, Esfahani JA. Numerical investigation of turbulent Cu-water nanofluid in heat exchanger tube equipped with perforated conical rings. Advanced Powder Technology. 2019;30(7):1338-47. doi:https://doi.org/10.1016/j.apt.2019.04.009

28. Cacua K, Buitrago-Sierra R, Herrera B, Pabón E, Murshed SMS. Nanofluids' stability effects on the thermal performance of heat pipes. Journal of Thermal Analysis and Calorimetry. 2019;136(4):1597-614. https://doi.org/10.1007/s10973-018-7787-5

29. Dippong T, Levei EA, Cadar O, Goga F, Toloman D, Borodi G. Thermal behavior of Ni, Co and Fe succinates embedded in silica matrix. Journal of Thermal Analysis and Calorimetry. 2019;136(4):1587-96. https://doi.org/10.1007/s10973-019-08117-8

30. Heidary H, Hosseini R, Pirmohammadi M, Kermani MJ. Numerical study of magnetic field effect on nanofluid forced convection in a channel. J Magn Magn Mater. 2015;374:11-7. https://doi.org/10.1016/j.jmmm.2014.08.001

31. Mousavi SV, Sheikholeslami M, Gorji bandpy M, Barzegar Gerdroodbary M. The Influence of magnetic field on heat transfer of magnetic nanofluid in a sinusoidal double pipe heat exchanger. Chem Eng Res Des. 2016; 113: 112-124. https://doi.org/10.1016/j.cherd.2016.07.009

32. Al-Balushi LM, Uddin MJ, Rahman MM. Natural convective heat transfer in a square enclosure utilizing magnetic nanoparticles. Propulsion and Power Research. 2019;8(3):194-209. https://doi.org/10.1016/j.jppr.2018.07.009

33. Alsabery AI, Mohebbi R, Chamkha AJ, Hashim I. Impacts of magnetic field and non-homogeneous nanofluid model on convective heat transfer and entropy generation in a cavity with heated trapezoidal body. Journal of Thermal Analysis and Calorimetry. 2019;138(2):1371-94. https://doi.org/10.1007/s10973-019-08249-x

34. Lee J-H, Jang J-t, Choi J-s, Moon SH, Noh S-h, Kim J-w et al. Exchange-coupled magnetic nanoparticles for efficient heat induction. Nat Nanotechnol. 2011;6(7):418-22. https://doi.org/10.1038/nnano.2011.95

35. Bitar A, Vega-Chacón J, Lgourna Z, Fessi H, Jafelicci M, Elaissari A. Submicron silica shell–magnetic core preparation and characterizatio. Colloids and Surfaces A: Physicochemical and Engineering Aspects. 2018;537:318-24. https://doi.org/10.1016/J.COLSURFA.2017.10.034.

36. Hu Y, Meng L, Niu L, Lu Q. Highly cross-linked and biocompatible polyphosphazene-coated superparamagnetic Fe_3O_4 nanoparticles for magnetic resonance imaging. Langmuir. 2013;29(29):9156-63. https://doi.org/10.1021/la402119s

37. Wei H, Bruns OT, Chen O, Bawendi MG. Compact zwitterion-coated iron oxide nanoparticles for in vitro and in vivo imaging. Integrative Biology. 2013; 5(1): 108-114.

38. Kurzhals S, Gal N, Zirbs R, Reimhult E. Aggregation of thermoresponsive core-shell nanoparticles: Influence of particle concentration, dispersant molecular weight and grafting. Journal of Colloid and Interface Science. 2017; 500: 321-332. http://doi.org/10.1016/j.jcis.2017.04.007

39. Puscasu E, Sacarescu L, Lupu N, Grigoras M, Oanca G, Balasoiu M, Creanga D. Iron oxide-silica nanocomposites yielded by chemical route and sol-gel method. J Sol-Gel Sci Techn. 2016; 79(3): 457-65. http://doi.org/10.1007/S10971-016-3996-1

40. Illés E, Szekeres M, Tóth IY, Szabó Á, Iván B, Turcu R, Vékás L, Zupkó I, Jaics G, Tombácz E. Multifunctional PEG-carboxylate copolymer coated superparamagnetic iron oxide

nanoparticles for biomedical application. J Magn Magn Mater. 2018; 451: 710-720. https://doi.org/10.1016/j.jmmm.2017.11.122

41. von der Lühe M, Weidner A, Dutz S, Schacher FH. Reversible Electrostatic Adsorption of Polyelectrolytes and Bovine Serum Albumin onto Polyzwitterion-Coated Magnetic Multicore Nanoparticles: Implications for Sensing and Drug Delivery. ACS Applied Nano Materials. 2018;1(1):232-44. http://doi.org/10.1021/acsanm.7b00118

42. Pflipsen C, Forge D, Benali S, Gossuin Y. Improved Stability and Relaxivity of a Commercial Magnetic Ferrofluid. J Phys Chem C. 2013; 117(40): 20919-20926. http://doi.org/10.1021/jp4050786

43. Jiemsakul T, Manakasettharn S, Kanharattanachai S, Wanna Y, Wangsuya S, Pratontep S. Microfluidic magnetic switching valves based on aggregates of magnetic nanoparticles: Effects of aggregate length and nanoparticle sizes. J Magn Magn Mater. 2017;422:434-9. http://doi.org/10.1016/j.jmmm.2016.09.040

44. Kallumadil M, Tada M, Nakagawa T, Abe M, Southern P, Pankhurst QA. Suitability of commercial colloids for magnetic hyperthermia. J Magn Magn Mater. 2009; 321(10): 1509-1513. http://doi.org/10.1016/J.JMMM.2009.02.075

45. Chaudhary RG, Juneja HD, Pagadala R, Gandhare NV, Gharpure MP. Synthesis, characterisation and thermal degradation behaviour of some coordination polymers by using TG–DTG and DTA techniques. Journal of Saudi Chemical Society. 2015;19(4):442-53. http://doi.org/10.1016/j.jscs.2014.06.002

46. Saville SL, Stone RC, Qi B, Mefford OT. Investigation of the stability of magnetite nanoparticles functionalized with catechol based ligands in biological media. Journal of Materials Chemistry. 2012;22(47):24909-17. http://doi.org/10.1039/C2JM34902G

47. Li Q, Wu L, Wu G, Su D, Lv H, Zhang S et al. New Approach to Fully Ordered fct-FePt Nanoparticles for Much Enhanced Electrocatalysis in Acid. Nano Letters. 2015;15(4):2468-73. http://doi.org/10.1021/acs.nanolett.5b00320

48. Lee DC, Mikulec FV, Pelaez JM, Koo B, Korgel BA. Synthesis and Magnetic Properties of Silica-Coated FePt Nanocrystals. The Journal of Physical Chemistry B. 2006;110(23):11160-6. http://doi.org/10.1021/jp060974z

49. Taboada E, Solanas R, Rodríguez E, Weissleder R, Roig A. Supercritical-Fluid-Assisted One-Pot Synthesis of Biocompatible Core(γ-Fe2O3)/Shell(SiO2) Nanoparticles as High Relaxivity T2-Contrast Agents for Magnetic Resonance Imaging. Advanced Functional Materials. 2009;19(14):2319-24. http://doi.org/10.1002/adfm.200801681

50. Green LAW, Thuy TT, Mott DM, Maenosono S, Kim Thanh NnT. Multicore magnetic FePt nanoparticles: controlled formation and properties. RSC advances. 2014;4(3):1039-44. http://doi.org/10.1039/C3RA44319A

51. Sathya A, Ravindran TR, Philip J. Superior thermal stability of polymer capped Fe3O4 magnetic nanoclusters. Journal of the American Ceramic Society. 2018;101(1):483-91. http://doi.org/10.1111/jace.15197

52. Vichery C, Maurin I, Bonville P, Boilot J-P, Gacoin T. Influence of Protected Annealing on the Magnetic Properties of γ-Fe2O3 Nanoparticles. The Journal of Physical Chemistry C. 2012;116(30):16311-8. http://doi.org/10.1021/jp305069a

53. Osterholtz FD, Pohl ER. Kinetics of the hydrolysis and condensation of organofunctional alkoxysilanes: a review. Journal of Adhesion Science and Technology. 1992; 6(1): 127-149. http://doi.org/10.1163/156856192X00106

54. Hong Y, Cha BJ, Kim YD, Seo HO. Mesoporous SiO2 Particles Combined with Fe Oxide Nanoparticles as a Regenerative Methylene Blue Adsorbent. ACS Omega. 2019;4(6):9745-55. http://doi.org/10.1021/acsomega.9b00726

55. Gao Y, Choudhury NR, Dutta N, Shanks R, Weiss R. Effect of the ionic aggregation on the crystallisation behavior of poly(ethylene) part of ionome. Journal of Thermal Analysis and Calorimetry. 2003;73(1):361-80. http://doi.org/10.1023/A:1025178818103

56. Pielichowski K, Flejtuch K. Phase Behavior of Poly(Ethylene Oxide) Studied by Modulated-Temperature DSC—Influence of the Molecular Weight. Journal of Macromolecular Science: Physics. 2004;43(2):459-70. http://doi.org/10.1081/MB-120029781

57. Khatiwada BK, Hetayothin B, Blum FD. Thermal Properties of PMMA on Silica Using Temperature- Modulated Differential Scanning Calorimetr. Macromolecular Symposia. 2013;327(1):20-8. http://doi.org/10.1002/MASY.201350502

58. Solarski S, Ferreira M, Devaux E. Characterization of the thermal properties of PLA fibers by modulated differential scanning calorimetry. Polymer. 2005;46(25):11187-92. http://doi.org/10.1016/j.polymer.2005.10.027.

59. de Almeida SH, Kawano Y. Thermal Behavior of Nafion Membranes. Journal of Thermal Analysis and Calorimetry. 1999;58(3):569-77. http://doi.org/10.1023/A:1010196226309.

60. Di Noto V, Gliubizzi R, Negro E, Pace G. Effect of SiO2 on Relaxation Phenomena and Mechanism of Ion Conductivity of [Nafion/(SiO2)x] Composite Membranes. The Journal of Physical Chemistry B. 2006;110(49):24972-86. http://doi.org/10.1021/jp0650331.

61. Vasquez ES, Chu IW, Walters KB. Janus Magnetic Nanoparticles with a Bicompartmental Polymer Brush Prepared Using Electrostatic Adsorption to Facilitate Toposelective Surface-Initiated ATRP. Langmuir. 2014;30(23):6858-66. http://doi.org/10.1021/la500824r.

62. SiMAG-basic. http://www.chemicell.com/products/microparticles/simag-basic/index.html. 2019. Accessed 10 Jan 2019.

63. Georgieva JV, Kalicharan D, Couraud P-O, Romero IA, Weksler B, Hoekstra D et al. Surface Characteristics of Nanoparticles Determine Their Intracellular Fate in and Processing by Human Blood-Brain Barrier Endothelial Cells In Vitro. Mol Ther. 2011;19(2):318-25. http://doi.org/10.1038/mt.2010.236.

64. Okhrimenko DV, Budi A, Ceccato M, Cárdenas M, Johansson DB, Lybye D et al. Hydrolytic Stability of 3-Aminopropylsilane Coupling Agent on Silica and Silicate Surfaces at Elevated Temperatures. ACS Applied Materials & Interfaces. 2017; 9(9): 8344-8353. http://doi.org/10.1021/acsami.6b14343.

65. Schaub NJ, Rende D, Yuan Y, Gilbert RJ, Borca-Tasciuc D-A. Reduced Astrocyte Viability at Physiological Temperatures from Magnetically Activated Iron Oxide Nanoparticles. Chem Res Toxicol. 2014;27(12):2023-35. http://doi.org/10.1021/tx500231f.

66. Shen X-C, Fang X-Z, Zhou Y-H, Liang H. Synthesis and Characterization of 3-Aminopropyltriethoxysilane-Modified Superparamagnetic Magnetite Nanoparticles. Chemistry Letters. 2004;33(11):1468-9.

67. Mahdieh A, Mahdavian AR, Salehi-Mobarakeh H. Chemical modification of magnetite nanoparticles and preparation of acrylic-base magnetic nanocomposite particles via miniemulsion polymerization. J Magn Magn Mater. 2017;426:230-8. http://doi.org/10.1016/j.jmmm.2016.11.091.

68. Maddumaarachchi M, Blum FD. Thermal analysis and FT-IR studies of adsorbed poly(ethylene-stat-vinyl acetate) on silica. Journal of Polymer Science Part B: Polymer Physics. 2014;52(10):727-36. http://doi.org/10.1002/polb.23476.

69. Yi L, Heitmann J, Scholz R, Zacharias M. Phase separation of thin SiO layers in amorphous SiO/SiO2 superlattices during annealing. Journal of Physics: Condensed Matter. 2003;15(39):S2887.

70. Piasek Z, Urbanski T. The infra-red absorption spectrum and structure of urea. B Pol Acad Sci-Tech X. 1962:113-20.

71. Pasternack RM, Rivillon Amy S, Chabal YJ. Attachment of 3-(Aminopropyl)triethoxysilane on Silicon Oxide Surfaces: Dependence on Solution Temperature. Langmuir. 2008;24(22):12963-71. http://doi.org/10.1021/la8024827.

72. Phan NTS, Jones CW. Highly accessible catalytic sites on recyclable organosilane-functionalized magnetic nanoparticles: An alternative to functionalized porous silica catalysts. Journal of Molecular Catalysis A: Chemical. 2006;253(1–2):123-31. http://doi.org/10.1016/j.molcata.2006.03.019.

73. Lummerstorfer T, Sohar C, Friedbacher G, Hoffmann H. In Situ Observation of Interfacial Bonding of an Organic Monolayer Confined between Two Solid Surfaces. Langmuir. 2006;22(1):18-21. http://doi.org/10.1021/la052307n.

74. Chiang C-H, Ishida H, Koenig JL. The structure of γ-aminopropyltriethoxysilane on glass surfaces. Journal of Colloid and Interface Science. 1980;74(2):396-404. http://doi.org/10.1016/0021-9797(80)90209-X.

75. Chiang C-h, Koenig JL. Fourier transform infrared spectroscopic study of the adsorption of multiple amino silane coupling agents on glass surfaces. Journal of Colloid and Interface Science. 1981;83(2):361-70. http://doi.org/10.1016/0021-9797(81)90331-3.